A Body Area Propagation Model Derived From Fundamental Principles: Analytical Analysis and Comparison With Measurements

Andrew Fort, *Member, IEEE*, Farshad Keshmiri, *Student Member, IEEE*, Gemma Roqueta Crusats, Christophe Craeye, *Member, IEEE*, and Claude Oestges

***Abstract*—Using wireless sensors worn on the body to monitor health information is a promising new application. To realize transceivers targeted for these applications, it is essential to understand the body area propagation channel. Several numerical, simulated, and measured body area propagation studies have recently been conducted. While many of these studies are useful for evaluating communication systems, they are not compared against or justified by more fundamental physical models derived from basic principles. This type of comparison is necessary to provide better physical insights into expected propagation trends and to justify modeling choices. To address this problem, we have developed a simple and generic body area propagation model derived directly from Maxwell's equations revealing basic propagation trends away, inside, around, and along the body. We have verified the resulting analytical model by comparing it with measurements in an anechoic chamber. This paper develops an analytical model of the body, describes the expected body area pathloss trends predicted by Maxwell's equations, and compares it with measurements of the electric field close to the body.**

***Index Terms*—Body area networks, propagation model.**

I. Introduction

WIRELESS bio-medical sensors are a promising new application made possible by recent advances in ultralow power technology [1]. Each sensor measures parameters of interest and sends the data in short bursts to a central device, such as a PDA. Both the sensors and the PDA are worn directly on the body. Examples include sensors to observe brain activity for recording or warning against seizure events, or sensors to examine heart activity for diagnosis and automatic emergency calls. The large diversity and potential of these applications makes it an exciting new research direction.

A computationally simple and generic body area propagation model is required to develop efficient low power radio systems for use near the human body. Measurements [2]–[5] and finite difference time domain (FDTD) simulations [6]–[8] have successfully described very specific communication scenarios. Using measured or simulated results, complete statistical ultrawideband and narrowband models have been developed in [9]–[11] and standardized by the IEEE [12]. These approaches are entirely appropriate for body area propagation modeling and have already proven effective for evaluating body area communication system proposals [13], [14]. However, measurements do not directly consider the physical propagation mechanism, forcing researchers to rely on some ad-hoc modeling approaches that are not always motivated by fundamental principles. On the other hand, realistic FDTD simulations that numerically evaluate the solution to Maxwell's equations of small antennas worn close to the sophisticated curved inhomogeneous human bodies are very time-consuming. Another approach is to use the uniform theory of diffraction (UTD) [15]. UTD is an extension to ray tracing allowing the propagation channel to be described in terms of the sum of rays diffracting around and reflecting from body parts [8]. While this approach offers considerable physical insight, it typically relies on a high-frequency asymptotic approximation which is not valid when the wavelength is of the same order of magnitude as the diffracting object, or for tangentially polarized antennas placed very close to the human body [15]. This scenario is particularly important for body worn antennas where it is desirable to have low-profile antennas for user comfort.

To help understand propagation near the body, we have implemented a computationally simple but generic model of body area propagation derived directly from Maxwell's equations. We assume the antenna can be modeled as a tangentially polarized point source, and the body can be modeled as a lossy cylinder, then evaluate the resulting electromagnetic fields. This approach is related to models developed for antennas printed on coated cylinders [16]–[19]. Unlike UTD, this exact computation is valid regardless of the distance of the antenna from the body and can be used for tangentially polarized antennas. The physical meaning of the main steps of this derivation is provided. We begin with the solution for an infinite line source in the vicinity of an infinite lossy cylinder. We then numerically calculate the inverse Fourier transform of the line source to obtain the fields due to a point source, representing the antenna, near a lossy cylinder, representing the body. Using this model, we have evaluated the electric fields for propagation around, along, away, and inside a lossy cylinder to estimate the major propagation trends near a human body, and we have proposed simple

Manuscript received November 25, 2007; revised February 13, 2009. First published June 23, 2009; current version published February 03, 2010.

A. Fort is with IMEC, B-3001 Leuven, Belgium and also with Vrije Universiteit Brussel (VUB), Dept. ELEC, B-1050 Brussels, Belgium (e-mail: forta@imec.be).

F. Keshmiri, C. Craeye, and C. Oestges are with Université Catholique de Louvain (UCL), B-1348 Louvain-La-Neuve, Belgium (e-mail: farshad.keshmiri@uclouvain.be; craeye@tele.ucl.ac.be; oestges@emic.ucl.ac.be).

G. R. Crusats is with Universitat Politècnica de Catalunya (UPC), 31 08034 Barcelona, Spain (e-mail: gemma.roqueta@tsc.upc.edu).

Digital Object Identifier 10.1109/TAP.2009.2025786

pathloss laws which can be used in practice. Finally, we have validated this approach by comparing the fields predicted by this simple model with actual measurements around the human body in an anechoic chamber. The resulting approach can therefore be used to rapidly approximate average pathloss near a body, or to physically justify the average pathloss trends of more realistic statistical models extracted from measurements and FDTD simulations.

This article summarizes our approach to analytical body area propagation modeling. Section II begins by outlining the various steps in our analytical developments. Section III reviews the well-known solution for a tangentially polarized line-source near a lossy conductor. To obtain a more realistic model of a small antenna close to the body, Section IV proposes a numerical integration technique to transform the line source into a point source and addresses other practical issues required for computer implementation. Section V demonstrates, from fundamental principles, the major pathloss trends expected for propagation near a curved lossy body and identifies some simplified pathloss laws which are more convenient to use in practice. Section VI then compares the total model with measurements taken near a body in an anechoic chamber. Finally, Section VII summarizes the major conclusions of this study.

II. Generic Approach to Body Area Modeling

Fig. 1 summarizes our proposed approach to body area modeling. We model the antennas as a point source with some polarity, and the human body as an infinite lossy cylinder with arbitrary material parameters. A point source is a reasonable approximation of an antenna if the antenna size is small compared with the wavelength. This is normally the case for compact body-worn devices. While this approximation is not appropriate for analyzing near-field propagation trends of realistic antennas, it can form the basis of future studies employing the method of moments. A lossy cylinder is a reasonable first order approximation of a human body allowing us to take into account many propagation phenomena, including diffraction around a curved lossy surface, reflections off the body, and penetration into the body. All of these effects are expected to play a role in body area propagation, though the relative importance of each effect will depend on such factors as the frequency, polarity, radius of curvature, and tissue properties. Thus, our chosen geometry will allow us to explore many important far-field body area propagation phenomena, while remaining analytically tractable so that a solution can be derived directly from fundamental principles.

In order to derive the electric fields around and inside a lossy cylinder resulting from a point source, we follow a two step procedure as indicated in Fig. 1. First, we solve the problem of a linear current source located outside a lossy cylinder. The solution to this problem can be obtained by representing the displaced cylindrical waves of the line source by a superposition of un-displaced cylindrical waves originating from the cylinder axis. This allows us to easily enforce the boundary conditions around the surface of the lossy cylinder. Section III describes the details of this step. Second, we convert the line source to a point source by performing an inverse Fourier transform of the current source along the vertical spectral coordinate (k_z). The transform must be obtained numerically using a contour integral to avoid a singularity in the line source solution. Section IV describes the details of this step. Throughout this article, we focus on the special case of a tangentially polarized point-source which is representative of low-profile antennas. Low profile antennas are more desirable for comfortable, low-cost body-worn devices. However, the general approach could also be used to investigate antennas polarized normal to the body having more desirable pathloss characteristics. We recommend this as future work.

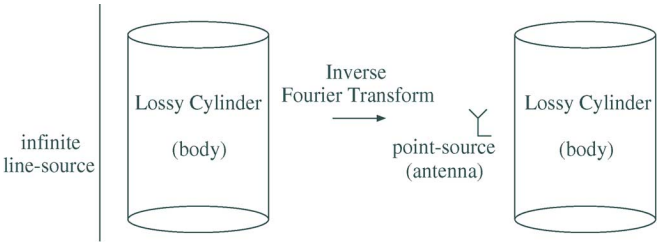

Fig. 1. Proposed two-step procedure for body area modeling. First we obtain the solution for a line-source near a lossy cylinder. Second, we transform the solution to a point source by taking its inverse Fourier transform.

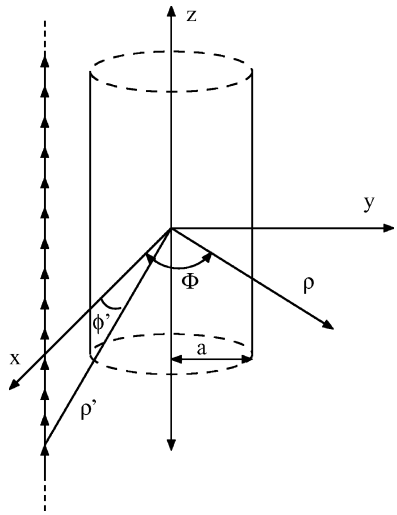

Fig. 2. Geometry and coordinate system for our analysis.

III. Line Source

Fig. 2 provides a more precise diagram of the geometry emphasizing the major variables used throughout our analysis. An infinite cylinder of radius a is oriented along the z-axis at the origin of the coordinate system. An infinite linear current source is located at cylindrical coordinates (ρ', ϕ'). We let the current on this line vary along the z-axis as $e^{-jk_z z}$. The exponent indicates the current source is a traveling wave in the $\hat{\mathbf{z}}$-direction with a propagation constant k_z. This choice of current will allow us to convert it to a point source by means of an inverse Fourier transform in Section IV.

We begin the body area modeling developments by writing down the well-known vector Helmholtz equations which are most convenient for solving this problem

$$(\nabla^2 + k^2)\mathbf{E} = j\omega\mu\mathbf{J}$$
$$(\nabla^2 + k^2)\mathbf{H} = -\nabla \times \mathbf{J} \quad (1)$$

where $k = \omega\sqrt{\mu\epsilon}$ is the wavenumber, ω is the angular frequency, μ is the material permeability, ϵ is material permittivity, and $\mathbf{J}$ is the current density.

We want to determine the electric field $\mathbf{E}$ and magnetic field $\mathbf{H}$ that satisfy (1) for the geometry shown in Fig. 2. We know that the general solution to this equation can be written as the sum of the solution to the homogeneous equation $(\nabla^2+k^2)\mathbf{E} = 0$ or $(\nabla^2 + k^2)\mathbf{H} = 0$, and any particular solution to (1). The solution to the homogeneous equation will correspond physically to the scattered field by the cylinder and will be discussed in Section III-A. The particular solution will correspond to the incident field from the line source propagating through free space without the presence of the lossy cylinder and will be discussed in Section III-B. Section III-C describes the total solution obtained by summing the scattered and incident fields and enforcing the boundary conditions along the surface of the cylinder.

A. Scattered Field

The z-component of the homogeneous solution to the Helmholtz equations for the electric and magnetic fields is obtained by separation of variables [16]

$$E_z^s(\rho,\phi,z) = \sum_{m=-\infty}^{+\infty} e^{jm\phi}e^{-jk_z z}\big(A_m J_m(k_\rho\rho)(1-U(\rho-a))_+ \times A'_m H_m^{(2)}(k_\rho\rho)U(\rho-a)\big) \quad (2)$$

where $U(\rho - a)$ as a delayed Unit step function set A to zero outside $(\rho > a)$ and A' to zero inside $(\rho < a)$ the cylinder. We also have

$$k_\rho = \sqrt{k^2 - k_z^2}. \quad (3)$$

Following the same reasoning, a similar expression can be derived for the magnetic field

$$H_z^s(\rho,\phi,z) = \sum_{m=-\infty}^{+\infty} e^{jm\phi}e^{-jk_z z}\left(B_m J_m(k_\rho\rho)\left(1-U(\rho-a)\right) + B'_m H_m^{(2)}(k_\rho\rho)U(\rho-a)\right) \quad (4)$$

$H_m^{(2)}$ and J_m represent the Hankel function of the second kind with order m and the Bessel function of the first kind with order m respectively. The constants A_m, A'_m, B_m, and B'_m will be determined in Section III-C from the boundary conditions imposed by the geometry. We will show later how the other components of the field can be obtained from the vertical components.

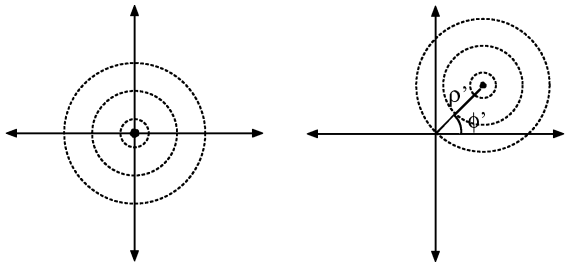

Fig. 3. The left side shows the wavefronts of an undisplaced cylindrical wave, while the right side shows the wavefronts of a displaced cylindrical wave that would be generated by a line source located at coordinates (ρ', ϕ').

B. Incident Field

The incident field can be determined by noting that the field everywhere, except on the current source itself, must take the form of the homogeneous solution in (2) since there are no current or charge sources in free-space. Thus, the $\hat{\mathbf{z}}$ component of the incident field will take the form

$$E_z^i(\rho,\phi,z) = \sum_{m=-\infty}^{+\infty} e^{jm\phi}e^{-jk_z z}\left(C_m J_m(k_\rho\rho)\left(1-U(\rho-\rho')\right) + C'_m H_m^{(2)}(k_\rho\rho)U(\rho-\rho')\right) \quad (5)$$

or

$$H_z^i(\rho,\phi,z) = \sum_{m=-\infty}^{+\infty} e^{jm\phi}e^{-jk_z z}\left(D_m J_m(k_\rho\rho)(1-U(\rho-\rho')) + D'_m H_m^{(2)}(k_\rho\rho)U(\rho-\rho')\right). \quad (6)$$

Physically, we expect the fields generated by the line-source to consist of displaced outgoing cylindrical waves originating from the line source at $\rho = \rho'$ (see Fig. 3). This expression indicates we can also express those fields by a sum of un-displaced cylindrical harmonics originating from the cylinder axis. The reason why we want to express the incident field solution as a sum of waves originating from the cylinder axis is that they have the same geometry as the lossy cylinder. This will make it easier to apply the boundary conditions of the complete solution at the surface of the cylinder in the following section.

We now need to determine the constants C_m and C'_m by applying the boundary conditions at the current source. The current source for the geometry shown in Fig. 2 can be expressed mathematically as

$$\mathbf{J^v} = \sum_{n=-\infty}^{+\infty} \frac{I_v e^{-jk_z z}}{\rho'}\delta(\rho-\rho')\delta(\phi - n2\pi)\hat{\mathbf{z}}. \quad (7)$$

Note that, without loss of generality, we have assumed that the source is located at $\phi' = 0$ and $z' = 0$, which will simplify our notation. We have also written this expression such that it is valid for $\phi \in (-\infty, +\infty)$. This requires the term $2n\pi$ (for all integers n) since our cylindrical geometry is periodic with ϕ

every 2π radians. The vector $\hat{\mathbf{z}}$ indicates a vertical polarization. For the horizontal polarization case, we will simply replace $\hat{\mathbf{z}}$ with $\hat{\boldsymbol{\phi}}$ and denote the current density and its amplitude as $\mathbf{J^h}$ and I_h respectively.

The current source representation in (7) will make it difficult to apply the boundary conditions since it has the form $e^{-jk_z z}$ while the incident field in (10) is expressed in terms of the sum of cylindrical harmonics of the form $e^{jm\phi}e^{-jk_z z}$. We will therefore transform our line source into a similar sum of cylindrical harmonics by applying the following Fourier transform pair

$$\sum_{n=-\infty}^{+\infty}\delta(\phi-n2\pi)\leftrightarrow\sum_{m=-\infty}^{+\infty}\delta(F-m) \tag{8}$$

resulting in the following expression:

$$\mathbf{J}=\frac{I}{2\pi\rho'}\delta(\rho-\rho')\sum_{m=-\infty}^{+\infty}e^{jm\phi}e^{-jk_z z}\hat{\mathbf{z}} \tag{9}$$

which now has the same mathematical form as (5). The source is now defined for all ϕ and is periodic every $\phi=2n\pi$, indicating a cylindrical current sheet. Thus, by using the Fourier Transform relation of (8), we have represented the original line source as a sum of cylindrical current sheets centered at the origin. This will allow us to easily apply the boundary conditions on the surface of the current sheet.

Since all expressions are now written using cylindrical harmonics having the form $e^{jm\phi}e^{-jk_z z}$ we will simply assume this term from now on without explicitly writing it every time. Furthermore, we introduce the following notation to represent a particular harmonic of propagation:

$$E^i_{m,z}(\rho,\phi,z)=\left(B_m J_m(k_\rho\rho)\left(1-U(\rho-\rho')\right)+B'_m H^{(2)}_m(k_\rho\rho)U(\rho-\rho')\right). \tag{10}$$

In this notation, $E^i_{m,z}$ represents the m^{th} harmonic of the incident field from (5). While we have not explicitly written the factor $e^{jm\phi}e^{-jk_z z}$, it is still there and we must remember to multiply the signal by jm or $-jk_z$ whenever we take its derivative with respect to ϕ or z.

We know that the Hankel function $H^{(2)}_m(k_\rho\rho)$ from (10) approaches infinity as $k_\rho\rho\to 0$. Since we cannot have infinite fields in practice, the portion of our geometry which includes the origin can only consist of Bessel functions. Similarly, the region outside our cylindrical sheet can only consist of Hankel functions. This allows us to re-write the incident field inside and outside the cylindrical current sheet as

$$E^i_{m,z}=\begin{cases}C_m J_m(k_\rho\rho) & \rho\le\rho'\\ C'_m H^{(2)}_m(k_\rho\rho) & \rho\ge\rho'\end{cases} \tag{11}$$

The expressions for the magnetic field have the same form, so we can also write the $\hat{\mathbf{z}}$-component of the magnetic field

$$H^i_{m,z}=\begin{cases}D_m J_m(k_\rho\rho) & \rho\le\rho'\\ D'_m H^{(2)}_m(k_\rho\rho) & \rho\ge\rho'.\end{cases} \tag{12}$$

We can determine the other components of the electromagnetic field from the vertical components using the following relations which are valid in any homogeneous medium, as proven from Maxwell's equations [16]:

$$\begin{aligned}\mathbf{E_s}&=\frac{1}{k_\rho^2}(-jk_z\nabla_s E_z+j\omega\mu\hat{z}\times\nabla_s H_z)\\ \mathbf{H_s}&=\frac{1}{k_\rho^2}(-jk_z\nabla_s H_z-j\omega\epsilon\hat{z}\times\nabla_s E_z)\end{aligned} \tag{13}$$

with

$$\begin{aligned}\nabla_s&=\hat{\rho}\frac{\partial}{\partial\rho}+\hat{\phi}\frac{jm}{\rho}\\ \hat{z}\times\nabla_s&=\hat{\phi}\frac{\partial}{\partial\rho}-\hat{\rho}\frac{jm}{\rho}\end{aligned} \tag{14}$$

The vectors $\mathbf{E_s}$ and $\mathbf{H_s}$ represent the $\hat{\boldsymbol{\phi}}$ and $\hat{\boldsymbol{\rho}}$ components of the electromagnetic field, while the scalars E_z and H_z represent the $\hat{\mathbf{z}}$ components. Applying this relation to (11) and (12) allows us to express the $\hat{\boldsymbol{\phi}}$ components as follows:

$$E^i_{m,\phi}=\begin{cases}\frac{1}{k_\rho^2}\Big(C_m\frac{mk_z}{\rho}J_m(k_\rho\rho)\\ \qquad+j\omega\mu k_\rho D_m J'_m(k_\rho\rho)\Big) & \rho\le\rho'\\ \frac{1}{k_\rho^2}\Big(C'_m\frac{mk_z}{\rho}H^{(2)}_m(k_\rho\rho)\\ \qquad+j\omega\mu k_\rho D'_m H^{(2)'}_m(k_\rho\rho)\Big) & \rho\ge\rho'\end{cases} \tag{15}$$

and

$$H^i_{m,\phi}=\begin{cases}\frac{1}{k_\rho^2}\Big(D_m\frac{mk_z}{\rho}J_m(k_\rho\rho)\\ \qquad-j\omega\epsilon_0 k_\rho C_m J'_m(k_\rho\rho)\Big) & \rho\le\rho'\\ \frac{1}{k_\rho^2}\Big(D'_m\frac{mk_z}{\rho}H^{(2)}_m(k_\rho\rho)\\ \qquad-j\omega\epsilon_0 k_\rho C'_m H^{(2)'}_m(k_\rho\rho)\Big) & \rho\ge\rho'.\end{cases} \tag{16}$$

Equations (11), (12) must satisfy the following tangential boundary conditions at the surface of the current sheets ($\rho=\rho'$):

$$E_{z1}=E_{z2} \tag{17}$$

$$E_{\phi1}=E_{\phi2} \tag{18}$$

$$\hat{\rho}\times(\mathbf{H_2}-\mathbf{H_1})=\mathbf{J} \tag{19}$$

The subscripts 1 and 2 indicate fields just inside and outside the current sheet respectively. The resulting solutions for a vertically and horizontally polarized current source are discussed

below. By adding together weighted combinations of these components, we can generate the solution for a point source having arbitrary tangential polarity.

1) Vertical Polarization: For the vertical polarity, the current source is polarized in the $\hat{\mathbf{z}}$ direction, as indicated in (9), resulting in the following solution:

$$C_m = -I_v \frac{k_\rho^2}{4\omega\epsilon} H_m^{(2)}(k_\rho \rho') \tag{20}$$

$$C'_m = -I_v \frac{k_\rho^2}{4\omega\epsilon} J_m(k_\rho \rho') \tag{21}$$

$$D_m = 0 \tag{22}$$

$$D'_m = 0. \tag{23}$$

2) Horizontal Polarization: The developments for the horizontally polarized current source proceed in the same manner as the vertically polarized current source except now the current sheets have a $\hat{\boldsymbol{\phi}}$ polarization instead of the $\hat{\mathbf{z}}$ polarization. This results in the following solution:

$$C_m = -I_h \frac{mk_z}{4\omega\epsilon\rho'} H_m^{(2)}(k_\rho \rho') \tag{24}$$

$$C'_m = -I_h \frac{mk_z}{4\omega\epsilon\rho'} J_m(k_\rho \rho') \tag{25}$$

$$D_m = -I_h k_\rho \frac{1}{4j} H_m^{(2)\prime}(k_\rho \rho') \tag{26}$$

$$D'_m = -I_h k_\rho \frac{1}{4j} J'_m(k_\rho \rho'). \tag{27}$$

For both the horizontal and vertical polarization cases, we have made use of the following well-known identity to write the result in this simple form [16]:

$$J'_m(x) H_m^{(2)}(x) - J_m(x) H_m^{(2)\prime}(x) = \frac{2j}{\pi x}. \tag{28}$$

C. Total Field

We have now developed the solution for the homogeneous equation in Section III-A, and a particular solution to the non-homogeneous equation in Section III-B. The general solution is the sum of these two solutions

$$\mathbf{E_m^t} = \mathbf{E_m^s} + \mathbf{E_m^i} \tag{29}$$

As indicated at the end of Section III-A, we still need to solve for the unknowns A_m, A'_m, B_m, and B'_m from (2)–(4) to determine the $\hat{\mathbf{z}}$ component of the scattered solution. We can re-write the field using the notation developed in Section III-B as

$$\begin{cases} E_{m,z}^t = A_m J_m(k_\rho \rho) & \rho \le a \\ E_{m,z}^s = A'_m H_m^{(2)}(k_\rho \rho) & \rho \ge a \end{cases} \tag{30}$$

and

$$\begin{cases} H_{m,z}^t = B_m J_m(k_\rho \rho) & \rho \le a \\ H_{m,z}^s = B'_m H_m^{(2)}(k_\rho \rho) & \rho \ge a. \end{cases} \tag{31}$$

Subscript m indicates the m^{th} harmonic and we implicitly assume the term $e^{jm\phi} e^{-jk_z z}$. As in the case of the incident field, we know the solution in the region inside the cylinder can only consist of Bessel functions while the region outside the cylinder can only consist of Hankel functions. The scattered and incident fields inside the cylinder have the same form so we combine these terms into E^t, which represents the total field, and assign it the constants A and A'. However, the scattered and incident fields outside the cylinder have a different form and cannot be combined together. We can also use the same approach to determine the $\hat{\boldsymbol{\phi}}$ from the vertical components by applying (13) to (30) and (31).

We can now solve for A_m, A'_m, B_m, and B'_m by applying the tangential boundary conditions of (17)–(19) to the surface of the cylinder at $\rho = a$. In our case, these boundary conditions state that the tangential fields just inside the cylinder equal the tangential fields just outside the cylinder. We can write this as follows:

$$\mathbf{E_{(1)}^t} = \mathbf{E_{(2)}^t} \tag{32}$$

$$\mathbf{E_{(1)}^t} = \mathbf{E_{(2)}^s} + \mathbf{E_{(2)}^i}$$

$$\mathbf{E_{(1)}^t} - \mathbf{E_{(2)}^s} = \mathbf{E_{(2)}^i} \tag{33}$$

where $\mathbf{E_{(2)}^s}$, $\mathbf{E_{(2)}^i}$ represent the scattered and incident tangential field components just outside the cylinder, and $\mathbf{E_{(1)}^t}$ represents the total field just inside the cylinder. Similar expressions can be written for the magnetic field. Finally, we can use our previous definitions of these various field components to re-write the second line of (33) in matrix format as follows:

$$\begin{bmatrix} J_{(1)} & -H_{(2)} & 0 & 0 \\ -\frac{F_\epsilon \epsilon_r}{k_{\rho 1}} J'_{(1)} & \frac{F_\epsilon}{k_{\rho 2}} H'_{(2)} & \frac{F_m}{k_{\rho 1}^2} J_{(1)} & -\frac{F_m}{k_{\rho 2}^2} H_{(2)} \\ \frac{F_m}{k_{\rho 1}^2} J_{(1)} & -\frac{F_m}{k_{\rho 2}^2} H_{(2)} & \frac{F_\mu \mu_r}{k_{\rho 1}} J'_{(1)} & -\frac{F_\mu}{k_{\rho 2}} H'_{(2)} \\ 0 & 0 & J_{(1)} & -H_{(2)} \end{bmatrix} \begin{bmatrix} A_m \\ A'_m \\ B_m \\ B'_m \end{bmatrix} = [E^i]$$

$$[E^i] = \begin{bmatrix} E_{m,z}^{iv} + E_{m,z}^{ih} \\ H_{m,\phi}^{iv} + H_{m,\phi}^{ih} \\ E_{m,\phi}^{iv} + E_{m,\phi}^{ih} \\ H_{m,z}^{ih} \end{bmatrix}. \tag{34}$$

On the right side of the equations, the terms E_m^{iv} and E_m^{ih} represent the incident fields for vertically and horizontally polarized line-sources with amplitudes I_v and I_h respectively. Their solution was already given in Section III-B. The left side of the equation is obtained from (30) and (31) using (13) to describe the $\hat{\boldsymbol{\phi}}$ components from the $\hat{\mathbf{z}}$ components. We have introduced the terms $F_m = mk_z/a$, $F_\mu = j\omega\mu$, $F_\epsilon = j\omega\epsilon_0$ to express the equation more compactly. Similarly, we have also introduced the notation $J_{(i)} = J_m(k_{\rho i} a)$ and $H_{(i)} = H_m^{(2)}(k_{\rho i} a)$, where $i = 1$ and $i = 2$ refer to the material just inside and outside the cylinder respectively.

We could solve (34) and express the constants A_m, A'_m, B_m, and B'_m in closed form. However, the resulting expressions are complicated and do not provide any additional insight. Therefore, we will simply solve the equation numerically when we implement the model on a computer in Section IV.

IV. Point Source

In the previous section, we developed the solution for a line source near a lossy cylinder. Our goal now is to convert the solution for a line-source into the solution for a point source. This can be accomplished using the following Fourier transform equivalence:

$$\delta(z) = \frac{1}{2\pi} \int_{-\infty}^{\infty} e^{-jk_z z} dk_z. \tag{35}$$

In our case, we can see that the left hand side of the equation could represent a point source. We could also interpret the right hand side of the equation to be a sum of line sources each having a current that is a traveling wave with a vertical propagation constant k_z. This, is the type of current source we considered in the previous section. From the linearity of Maxwell's equations, we know that the combined field due to several sources is equal to the sum of the fields of each individual source. Therefore, we can write the following:

$$\begin{aligned} \mathbf{E^{pt}} &= \frac{1}{2\pi} \int_{-\infty}^{\infty} \mathbf{E^t} dk_z \\ &= \frac{1}{2\pi} \int_{-\infty}^{\infty} \sum_{m=-\infty}^{\infty} \left(\mathbf{E_m^s} + \mathbf{E_m^i} \right) dk_z. \end{aligned} \tag{36}$$

The vector $\mathbf{E^{pt}}$ represents the field due to a point source.

It is too difficult to perform the integration of (36) analytically, so we must resort to a numerical integration by computer. Unfortunately, this is complicated by the presence of a pole in the line source solution when $k_z = k_0$. This pole can be seen by noting $k_\rho = \sqrt{k_0^2 - k_z^2}$ as indicated in (3). Thus, $k_\rho \to 0$ when $k_z \to k_0$ which will cause the various Hankel functions in our solution to approach infinity. There may be other poles resulting from the solution of (34). To avoid these singularities in the line-source solution, we can perform a contour integral in the complex plane around the singularity at $k_z = k_0$. We have found that a parabolic contour, defined as in Fig. 4, together with Simpson's rule, provides a practical numerical integration technique that rapidly converges to a good approximation of the solution. This contour integral can be expressed as

$$b = C \left(1 - \left(\frac{a - k_0}{k_0} \right)^2 \right). \tag{37}$$

We must carefully choose the parameter C defining the height of the parabolic contour in Fig. 4. If C is too small, then the contour gets too close to the singularity and the integral becomes difficult to evaluate numerically. On the other hand, if C is too large, then the Hankel functions become difficult to evaluate since they increase exponentially with $Im\{k_z\}$. An exact numerical analysis of this problem is beyond the scope of this article. Instead, we have simply plotted the integrand and chosen the contour integration parameters to produce a smooth result. Typically, C is chosen to be a positive number less than 0.01.

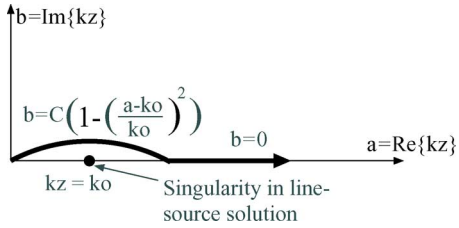

Fig. 4. A parabolic contour around the singularity at $k_z = k_0$ is a good numerical method for evaluating the inverse Fourier transform when converting to a point source.

Finally, we can only evaluate a finite number of terms to calculate the summation over m. This can be problematic since routines for computing Hankel functions may exhibit numerical overflow problems for large m and small complex or real arguments. Fortunately, this numerical aspect of the problem has already been investigated. A simple recursive formula for obtaining the largest calculable m for Hankel functions has been derived in [20] and can be used to approximate an appropriate number of terms in the summation. Typically, less than 200 terms are required for an accurate solution.

V. Body Area Pathloss Trends

We have implemented the analytical model of a point source near a lossy cylinder described in Section IV. We are now able to use these expressions to calculate basic pathloss trends around an arbitrary cylinder much faster than with FDTD. Section V-A investigates propagation trends away from and into the lossy cylinder. Section V-B investigates propagation trends along and around the surface of a lossy cylinder. We will compare these results with actual measurements around a human body in Section VI.

A. Propagation Away and Into a Lossy Cylinder

Fig. 5 shows the electric field magnitude expressed in dBV/m as a function of observation radius for a point source just outside a lossy cylinder[1]. It shows the field values for both a 400 MHz and a 2.45 GHz source. In both cases, the point source is located at $\rho' = 0.16$ meters. The lossy cylinder is centered at the origin and has a radius of $a = 0.15$ meters which roughly corresponds to the radius of a typical human torso. It is indicated on the figure with dashed lines. The source is therefore just one centimeter away from the cylinder on the right side. We set the material properties of the cylinder according to the high-water content human tissues in Table I.

The electric field away from the cylinder on the right side of the figure decays proportionally with distance ($|E|^2 \propto d^{-2}$) as expected in free space. The electric field into the cylinder between the dashed lines is roughly a straight line on our log-linear

[1]dBV/m is $20log10(E)$ and represents the magnitude of the electric field in dB relative to 1 V/m

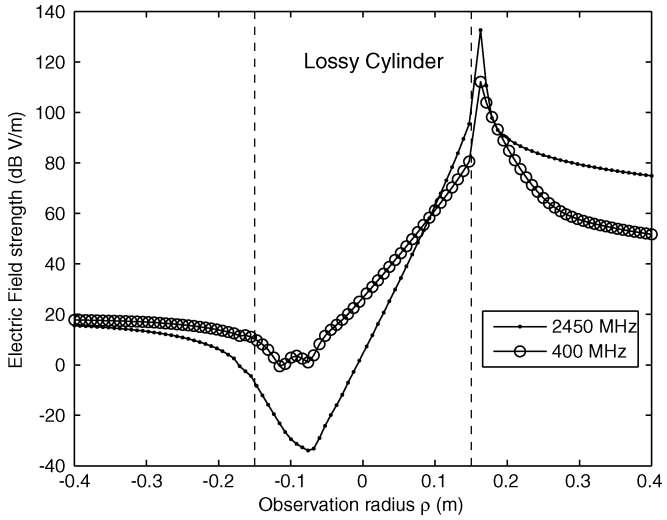

Fig. 5. Electric field as a function of observation radius for a point source just outside a lossy cylinder. A 1 Amp point source is located at $\rho = 0.16$ meter on the right side of the figure. The lossy cylinder is shown with dashed lines.

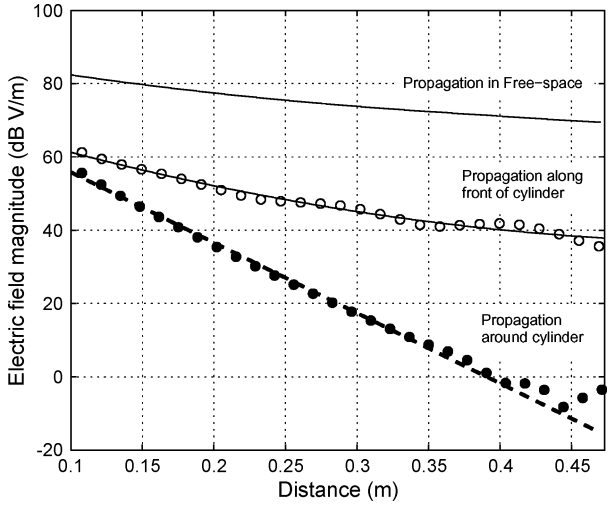

Fig. 6. Electric field as a function of distance through free-space, along the length of the cylinder, and around the cylinder. The lossy cylinder radius is 0.15 m, and both the observation and source radii are 1 centimeter away from the cylinder. All results are for a frequency of 2.45 GHz and a 1 Amp current.

TABLE I
ELECTRIC PROPERTIES OF HUMAN TISSUES WITH HIGH WATER CONTENT SUCH AS MUSCLE AND SKIN [21]

Frequency (MHz)	*Wavelength in air (cm)*	*Dielectric Constant* (ϵ_H)	*Conductivity* σ_H *(mho/m)*	*Wavelength* λ_H *(cm)*
400	69.3	53	1.43	8.76
915	32.8	51	1.60	4.46
2450	12.2	47	2.21	1.76
6000	5.17	43.3	4.73	0.775

scale indicating it decays exponentially with distance ($E \propto \exp(-d)$). This is also not surprising since the waves are propagating through a lossy medium and therefore decay exponentially [22]. As expected, the electric field decays more rapidly at 2.45 GHz than at 400 MHz since the skin depth is proportional to the square root of the wavelength [22]. This effect is compounded by the fact that body tissues of high water content tend to be better conductors at higher frequency. As expected, the field values on the opposite side of the cylinder are much lower since they are more shadowed by the cylinder.

Fig. 5 shows that there is a local minimum of the electric field inside the cylinder. The field decays roughly exponentially on either side of this minimum. This behavior suggests that, at high frequencies, the fields on the opposite side of the body will result from diffraction *around* the surface of the body rather than penetration *through* the body. This occurs because the body is a relatively good conductor. These results have also been verified with FDTD simulations on more sophisticated models of the body incorporating heterogeneous tissues [23].

Finally, the left side of Fig. 5 shows how tangential fields decay rapidly close to the surface of a lossy conductor. For example, the fields on the left edge of the figure are actually higher than the fields next to the cylinder even though they are physically much further away from the antenna. If bodies were perfect conductors, the electric field would vanish on the surface completely. The human body is actually an imperfect conductor, so there will be some tangential component to the electric field. Nevertheless, we can expect this field component to decay rapidly close to the body surface resulting in higher pathloss. Note that a normally polarized electric field would not decay close to the surface of a conductor in the same manner indicating that antenna polarization will have a fundamental impact on body area propagation and hence communication performance.

B. Propagation on the Surface of a Lossy Cylinder

Fig. 6 shows the electric field magnitude expressed in dB V/m as a function of distance for a 2.45 GHz point source. As before, the lossy cylinder has a radius of $a = 0.15$ meters. The point source is located just 1 centimeter away from the body at $\rho' = 0.16$ meters. Three curves are presented. The top curve shows the electric field versus distance for a point source in free space. The middle curve shows the electric field versus distance along the front surface of the cylinder. The bottom curve shows the electric field versus distance *around* the surface of the cylinder. The top two curves are obtained using a horizontally polarized point source and calculating the electric field along the $\hat{\mathbf{z}}$ direction. For the top curve, we set the material properties of the lossy cylinder to the properties of free space. For the middle curve, we set the lossy cylinder properties according to the high water content tissues of Table I. The bottom curve was obtained by using a vertically polarized point source and varying the angle of observation $\hat{\boldsymbol{\phi}}$. In all cases, the observation radius is set to the radius of the source ($\rho = \rho' = 0.16$ m).

We can see from Fig. 6 that the two curves along and around the surface of the cylinder (shown with circles and dots respectively) are shifted down compared with the free space curve. As explained in the previous section, this is because we expect the tangential fields to be small close to a lossy conductor compared with fields in free space. It is also clear that we can expect the pathloss versus distance trend on a body to be very sensitive to the trajectory we consider. The electric field will decay significantly more rapidly when considering propagation around a

body into the shadow region compared with propagation along the front of a body.

The middle curve, representing propagation along the front surface of the cylinder, decays somewhat faster than in free space. In free space, $|E|^2 \propto d^{-2}$ while we have found that $|E^2| \propto d^{-m}$ with m between 3–3.5 provides a reasonable approximation for different frequencies and radii. The excellent fit of this power law relationship is shown by the dashed line. It is difficult to provide a physical interpretation of this trend other than to say it is a consequence of Maxwell's Equations. We can suggest that higher pathloss trends are normally expected near conducting surfaces due to material losses. However, given the close proximity of the source and lossy surface, other contributions such as surface waves may also influence results.

The bottom curve representing propagation around the cylinder is approximately a straight line on our log-linear scale indicating it decays roughly exponentially with distance ($|E|^2 \propto \exp(-\alpha d)$). The excellent fit of an exponential decay law is shown by the dashed line. The exponential decay is not obvious from our developments in Sections III, IV since the model is expressed in terms of Hankel and Bessel functions. However, high-frequency asymptotic approximations for diffraction around curved conducting surfaces based on the uniform theory of diffraction (UTD) also tend to decay exponentially with distance [15]. In this case, waves guided by a curved surface are often called *creeping waves*. Unfortunately, we do not know of any suitable UTD approximations valid for tangentially polarized sources close to a conducting surface[2]. This is because the source and surface are very close with respect to the wavelength we consider. UTD approximations are only valid when the geometry does not vary significantly over an interval on the order of a wavelength [15]. Nevertheless, we propose that the exponential decay our model predicts can be interpreted as creeping waves diffracting around curved surfaces and suggest as future work finding suitable approximations to show this analytically for our geometry. For creeping wave propagation, the rapid attenuation around the body is related to the continuous shedding of energy tangent to the cylinder as a wave rotates around the surface into the shadowed region [15]. Thus, energy is radiated away from the body during the diffraction process which results in a faster pathloss versus distance trend close to the surface of the body. The fluctuation of the curve near the back of the body can be interpreted as the interference of clockwise and counter-clockwise creeping waves. Fig. 7 shows the pathloss versus distance trend for propagation around the same 0.15 m radius cylinder at different frequencies. The pathloss is shown in dB relative to the pathloss at a reference distance of 0.1 meters. In general, the rate of exponential decay increases with frequency around a lossy cylinder which is also consistent with creeping wave diffraction [15]. We also see that the curves tend to flatten out on the opposite side of the body with respect to a perfect exponential decay, especially at lower frequencies. This is likely due to clockwise and counter-clockwise diffracting waves interfering with each other on opposite sides of the cylinder.

[2]On the other hand, UTD approximations valid for normally polarized sources located on perfectly conducting surfaces are well known [15] and have even been employed in body area propagation studies [8]

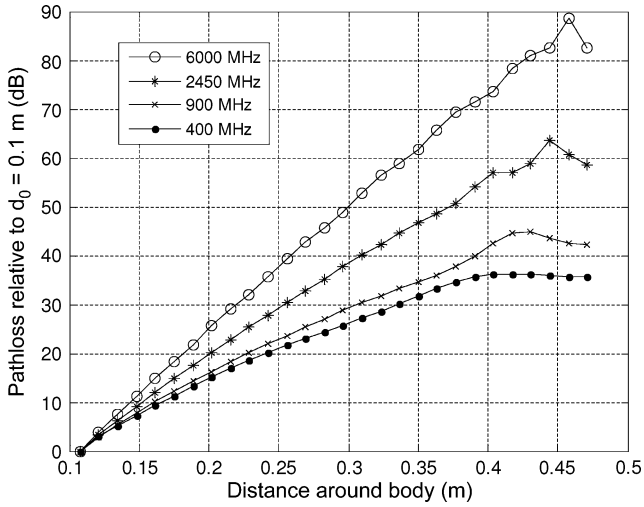

Fig. 7. Propagation around a lossy cylinder at different frequencies.

VI. Comparison With Measurements

Obviously, the geometry considered in the previous sections does not perfectly represent an antenna and body. Thus, we have compared the pathloss trends predicted by our simplified lossy-cylinder model with measurements of the electric field close to the human body using actual antennas. Section VI-A describes our measurement setup, while Section VI-B compares our model and measurement results.

A. Measurement Setup

An HP8753ES vector network analyzer (VNA) is used to measure the S21 parameter between two antennas placed at various positions on a human body in an anechoic chamber. The two antennas are connected to the VNA using 6 meter low-loss coaxial cables. Measurements are taken at 915 MHz and 2.45 GHz. We focus on these frequencies since they represent unlicensed ISM bands available internationally [24], and are also used by recent narrowband standardization efforts such as Zigbee [25] and Bluetooth [26].

The same small, low-profile Skycross SMT-8TO25-MA [27] antennas are used for all measurements. The antennas are 50.5 by 28 by 8 mm in size and weigh only 4.2 grams. These antennas were chosen since they are close to the size and profile requirements typical of comfortable body worn sensor devices [1]. Furthermore, they have a wide bandwidth which minimizes degradation resulting from the antenna being de-tuned when placed near the body [28].

The distance between the body and the antenna can significantly influence the pathloss and needs to be carefully controlled [3]. We control this separation by putting a 5 mm dielectric between the body and the antenna. In the same manner as [9], the antenna is taped to this dielectric and held against the body using tight elastics so they can not move while a measurement is being made. In all cases, the antennas are mounted so they are vertically polarized parallel to the body surface.

We analyze the antenna matching by measuring the S_{11} parameter in free-space and close to the body. In free space, the

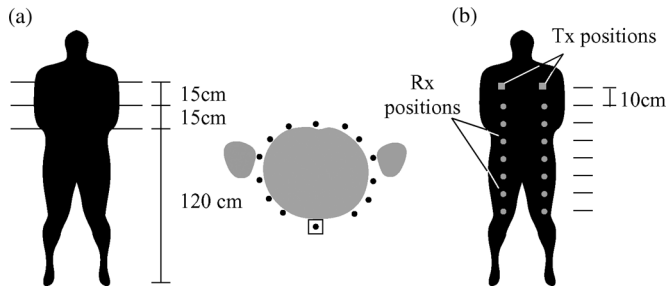

Fig. 8. Experimental setup: measurement locations around body.

S_{11} parameter is below -10 dB across the band of interest indicating the measurement setup itself does not introduce significant matching loss. When mounted on the body, the S_{11} parameter can vary depending on the placement of the antenna on the body. It remains good at 915 MHz ($S_{11} < -10$ dB) but in some cases becomes marginal at 2.4 GHz ($S_{11} < -5$ dB). It is possible that the coaxial cable and connector may radiate energy influence the pathloss versus distance trends. However, the display on our VNA remains stable when we move the cables indicating they do not radiate enough energy to appreciably alter our results.

Fig. 8(a) shows where the antennas are placed around the torso. All channel parameters are extracted from measurements performed in 3 planes separated by approximately 15 cm along the vertical axis (see left diagram). The right diagram shows where the antennas are placed for each plane. The receiver positions are marked with circles, while the transmitter is marked with a box around the circle. The transmitter is always placed on the front, and the receiver is placed at distances of 10–45 cm in steps of 5 cm measured around the perimeter of the body.

Fig. 8(b) shows where the antennas are placed for communication along the torso. The transmitter is worn at approximately shoulder height at one of two different positions. The receiver is placed directly below the transmitter at seven positions separated by 10 cm covering the range from the shoulder to the knees. To gather more measurement points, we repeat the procedure on the back of the body.

B. Measurement and Model Comparison

Fig. 9 compares the pathloss versus distance measured around the body and along the body for 2.45 GHz and 915 MHz frequencies with the analytical model developed in Sections III, IV. The vertical axis represents the pathloss. The horizontal axis is the distance traveled by the wave around or along the surface of the body. The circles indicate individual measurements, while the solid line was calculated using our physical model derived from Maxwell's equations. The torso used in this experiment has a radius of between 13–15 cm depending on the height at which the measurement is made. Thus, we use a cylinder radius of $a = 14$ centimeters and placed the antenna and observation point at $\rho' = 14.5$ centimeters away from the lossy cylinder in our analytical model. Furthermore, we set the material properties to the high-water content tissues of Table I. Since a point source does not exhibit the same near-field losses as the antenna used in our experiment, the analytical results are normalized to minimize the mean squared error.

The analytical model of a lossy cylinder matches the average trends of the measurements around a real body remarkably well considering the gross simplification of the body shape and antenna. As predicted by Maxwell's Equations, propagation around the body results in a more rapid attenuation versus distance trend than propagation along the body. However, there is a large variance in the pathloss measured at a particular distance around the torso consistent with other measured and simulated results [8]. This variance can be attributed to several physical factors including random interaction of the antenna and body at different locations, reflections off the arms, and variations in the local curvature or tissue properties. Since our analytical model is based on a uniform lossy cylinder and does not incorporate antenna losses, we can not expect it to take into account these fluctuations. This effect is better analyzed using statistical models based on either measurements or FDTD simulations. Some researchers have proposed modeling these contributions using a log-normal random variable since many of the effects are multiplicative [8], [10], [11].

Comparing the top two figures with the bottom two figures, it is clear that the pathloss within 10–20 centimeters of the antenna is significantly lower at 915 MHz than at 2.45 GHz. This indicates that the losses for these particular antennas are lower at 915 MHz than at 2.45 GHz. Part of this can be explained by the higher matching losses at 2.45 GHz compared with 915 MHz. Furthermore, at least in free-space, the antennas are constant gain (non-constant aperture) between 800 MHz–2.45 GHz resulting in an attenuation of higher frequencies. However, the antenna properties are also affected by the nearby body and propagation is along the body surface rather than through free-space.

Finally, similar pathloss trends for tangentially polarized antennas have been reported in the literature consistent with our theoretical derivations [2], [10], [11]. However, pathloss measurements in office building rather than in an anechoic chamber tend to flatten out on the back of the body in comparison with Fig. 9 due to the presence of nearby scatterers [2], [9], [11], and can also exhibit small-scale fading due to the interference of diffracting components near the body with reflections from nearby scatterers [11]. For narrowband systems, Ricean and Rayleigh small-scale fading models can be used depending on the amount of shadowing [11]. For ultrawideband systems, modified Saleh-Valenzuela models can be used to incorporate later arriving multipath clusters [9], [29].

VII. Conclusions and Future Work

We have proposed a simplified physical body area propagation model derived directly from Maxwell's equations. The model assumes the body can be approximated as an infinite lossy cylinder and the antenna can be approximated as a point source just outside the cylinder. A complete derivation starting from Maxwell's equations was developed together with a practical numerical method for evaluating it on a computer. We then used this model to identify the following approximate body area propagation trends which can be used to justify more sophisticated empirical models:

- $|E|^2 \propto d^{-2}$ away from the body;
- $|E|^2 \propto \exp(-\alpha d)$ into the body;
- $|E|^2 \propto \exp(-\beta d)$ around the body;

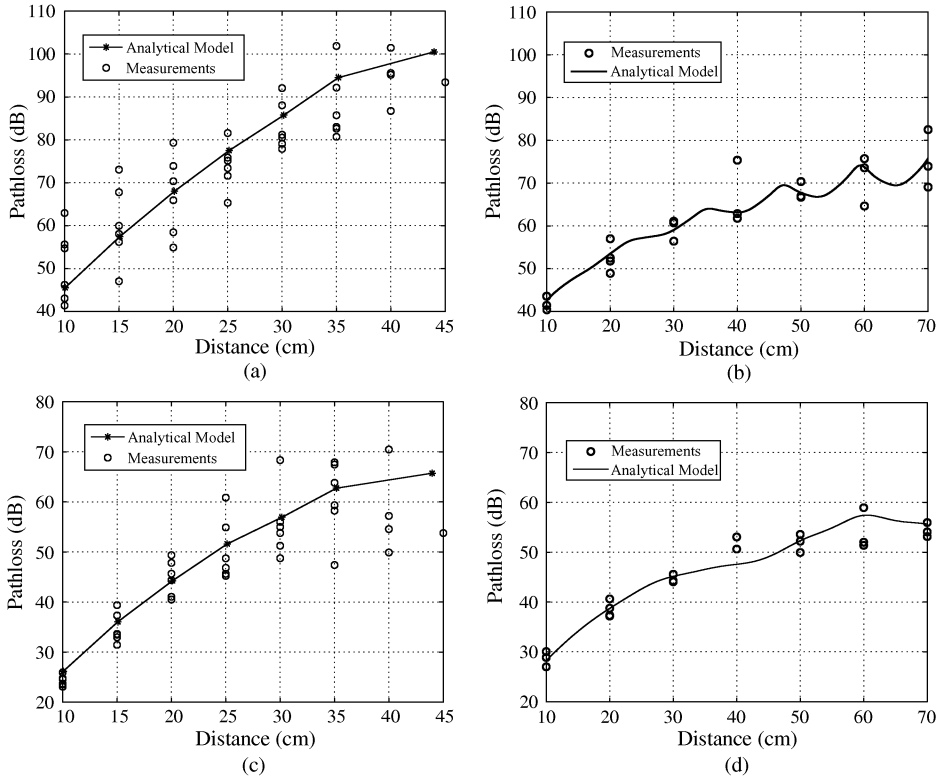

Fig. 9. Comparison of the analytical model for propagation around/along a cylinder and measurements around/along a real human body in an anechoic chamber. (a) 2450 MHz, around torso; (b) 2450 MHz, along front of torso; (c) 915 MHz, around torso; (d) 915 MHz, along front of torso.

- $|E|^2 \propto d^{-m}$ along the body with $m \approx 3$–3.5

The electric field (E) is inversely proportional to the distance away from the body in free space. However, the field has a much more rapid exponential decay into and around the body. The exponential decay into the body is expected in a lossy medium. The exponential decay around the body is typical of creeping wave propagation around conducting surfaces. Along the front of the body, the pathloss versus distance decays more rapidly than in free space but does not follow the same rapid exponential trends as propagation around the body. The decay rates (α, β, and m) depend on several factors including the tissue properties, frequency, polarity, and proximity to the body. While they cannot be evaluated directly, they can be estimated easily from our analytical model much faster than with numerical simulation methods such as FDTD. In general, normal polarization, lower frequency, and increasing the body-antenna separation will result in more desirable pathloss trends from an electromagnetic perspective. Unfortunately, these trends are less desirable from an application perspective where we desire small, low-profile antennas worn directly against the body. Thus, emerging body area communication systems will need to find a good compromise between these conflicting constraints.

For the first time, we have shown how the average pathloss trends of small tangentially polarized antennas measured in an anechoic chamber closely follow the trends predicted from Maxwell's Equations for propagation around and along a lossy cylinder. As predicted, pathloss due to diffraction around the body is significantly higher than pathloss along the body. There is a large variance in the pathloss measured at a particular distance around the torso. This variance can be attributed to several physical factors including random interaction of the antenna and body at different locations, reflections off the arms, and variations in the local curvature or tissue properties.

Our modeling approach is very generic and we can recommend several future uses and extensions. Frequency dispersion and pathloss trends can be investigated for ultrawideband propagation systems by evaluating the fields across several different frequencies. Furthermore, by using different Fourier Transform relations, the line-source solution can be converted to different current density patterns more representative of practical antennas such as finite length dipoles. Finally, the model can be used as a Green's function in an integral equation and solved using the method of moments to predict the fields near a lossy cylinder generated by practical three-dimensional antennas. This approach is computationally faster than FDTD at the cost of a simplified body model. However, considering that all bodies are different, an exact calculation of electric field values near a particular body model may not provide significantly more insight than a cylindrical approximation. Furthermore, if more precise field values are necessary, FDTD methods can be used to fine-tune or verify antenna parameters obtained more easily with the method of moments.

REFERENCES

[1] B. Gyselinckx, C. V. Hoof, and S. Donnay, "Body area networks, the ascent of autonomous wireless microsystems," presented at the Int. Symp. on Hardware Technol. Drivers of Ambient Intelligence, 2004.

[2] T. Zasowski, F. Althaus, M. Stager, A. Wittneben, and G. Trõster, "UWB for noninvasive wireless body area networks: Channel measurements and results," in *Proc. IEEE Conf. on Ultra Wideband Systems and Technol.*, 2003, pp. 285–289.

[3] A. Fort, C. Desset, J. Ryckaert, P. De Doncker, L. Van Biesen, and P. Wambacq, "Characterization of the ultra wideband body area propagation channel," in *Int. Conf. on Ultra-Wideband (ICU) Proc.*, Zurich, Sep. 2005, pp. 22–27.
[4] P. Hall, M. Ricci, and T. Hee, "Measurements of on-body propagation characteristics," in *Int. Conf. on Microw. and Millimeter Wave Technol.*, 2002, pp. 770–772.
[5] A. Alomainy, Y. Hao, X. Hu, C. G. Parini, and P. S. Hall, "UWB on-body radio propagation and system modelling for wireless body-centric networks," *IEE Commun. Proc.*, vol. 153, no. 1, pp. 107–114, Feb. 2006.
[6] W. Scanlon and N. Evans, "Numerical analysis of bodyworn UHF antenna systems," *Electron. Commun. Engineering J.*, vol. 13, no. 2, pp. 53–64, 2001.
[7] J. Ryckaert, P. DeDoncker, S. Donnay, A. Delehoye, and R. Meys, "Channel model for wireless communication around the human body," *Electron. Lett.*, vol. 40, no. 9, pp. 543–544, Apr. .
[8] Y. Zhao, Y. Hao, A. Alomainy, and C. Parini, "UWB on-body radio channel modeling using ray theory and subband FDTD method," , vol. 54, no. 4, pp. 1827–1835, Jun. 2006.
[9] A. Fort, J. Ryckaert, C. Desset, P. De Doncker, and L. Van Biesen, "Ultra wideband channel model for communication around the human body," *IEEE J. Sel. Areas Commun.*, 2006.
[10] A. Fort, C. Desset, P. De Doncker, and L. Van Biesen, "An ultra wideband body area propagation channel model: From statistics to implementation," *IEEE Trans. Microw. Theory Tech.*, 2006.
[11] A. Fort, P. Wambacq, C. Desset, and L. V. Biesen, "An indoor body area channel model for narrowband communications," *IET Microw. Antennas Propag.*, to be published.
[12] A. F. Molisch, D. Cassioli, C.-C. Chong, S. Emami, A. Fort, B. Kannan, J. Karedal, J. Kunisch, H. G. Schantz, K. Siwiak, and M. Z. Win, "A comprehensive standardized model for ultrawideband propagation channels," *IEEE Trans. Antennas Propag.*, vol. 54, no. 11, pp. 3143–3150, Nov. 2006.
[13] A. Fort, C. Desset, P. Wambacq, and L. Van Biesen, "Body area RAKE receiver communication," presented at the IEEE Conf. on Commun. (ICC), Turkey, 2006.
[14] A. Fort, M. Chen, C. Desset, P. Wambacq, and L. Van Biesen, "Impact of sampling jitter on mostly-digital architectures for UWB bio-medical applications," presented at the IEEE Conf. on Commun. (ICC), Glascow, 2007.
[15] D. A. Mcnamara, C. Pistorius, and J. Malherbe, *Introduction to the Uniform Geometrical Theory of Diffraction*. Boston, MA: Artech House, 1991.
[16] W. C. Chew, *Waves and Fields in Inhomogeneous Media*. New York: IEEE Press, 1995.
[17] V. B. Erturk and R. G. Rojas, "Efficient computation of surface fields excited on a dielectric coated circular cylinder," *IEEE Trans. Microw. Theory Tech.*, vol. 48, no. 10, pp. 1507–1516, 2000.
[18] J. Sun, C. F. Wang, L. W. Li, and M. S. Leong, "Further improvement for fast computation of mixed potential Green's functions for cylindrically stratified media," *IEEE Trans. Antennas Propag.*, vol. 52, no. 11, pp. 3026–3036, 2004.
[19] S. Raffaelli, Z. Sipus, and P. S. Kildal, "Analysis and measurements of conformal patch array antennas on multilayer circular cylinder," *IEEE Trans. Antennas Propag.*, vol. 53, no. 3, pp. 1105–1113, 2005.
[20] C. F. du Toit, "A procedure for determining the largest computable order of bessel functions of the second kind and hankel functions," *IEEE Trans. Antennas Propag.*, vol. 41, no. 12, pp. 1741–1742, Dec. 1993.
[21] C. C. Johnson and A. W. Guy, "Nonionizing electromagnetic wave effects in biological materials and sytems," *Proc. IEEE*, vol. 60, no. 6, pp. 692–718, Jun. 1972.
[22] D. K. Cheng, *Field and Wave Electromagnetics*, 2nd ed. Reading, MA: Adisson-Wesley Publishing Company, 1992.
[23] A. Fort, C. Desset, J. Ryckaert, P. DeDoncker, L. Van Biesen, and S. Donnay, "Ultra wide-band body area channel model," in *Int. Conf. Commun. (ICC) Proc.*, Seoul, Korea, May 2005, vol. 4, pp. 2840–2844.
[24] International Telecommunications Union—Radiocommunications (ITU-R), Radio Regulations, Section 5.138 and 5.150 [Online]. Available: http://www.itu.int/home
[25] IEEE, IEEE 802.15.4, Wireless Medium Access Control (MAC) and Physical Layer (PHY) Specifications for Low-Rate Wireless Personal Area Networks (LR-WPANs) October 2003.
[26] The Bluetooth Standard Version 1b [Online]. Available: http://www.bluetooth.com
[27] Skycross [Online]. Available: http://www.skycross.com
[28] W. G. Scanlon, N. E. Evans, and M. Rollins, "Antenna-body interaction effects in a 418 MHz radio telemeter for infant use," in *18th Annu. Int. Conf. of the IEEE Eng. in Medicine and Biology Society*, 1996, pp. 278–279.
[29] A. Saleh and R. A. Valenzuela, "A statistical model for indoor multipath propagation," *IEEE J. Sel. Areas Commun.*, vol. 5, no. 2, pp. 128–137, Feb. 1987.

Andrew Fort (S'04–M'07) was born in Ottawa, ON, Canada, in 1975. He received the Bachelor's degree in computer and electrical engineering from the University of Victoria, Canada, in 1998 and the Ph.D. degree in applied sciences (with greatest distinction) from the Free University of Brussels, Belgium, in 2007.

Between 1998 and 2000, he worked with IVL Technologies, Canada, researching real-time DSP algorithms for pitch recognition of the human voice. He joined IMEC, Belgium, in January 2000 and spent seven years researching and developing of a wide range of communication systems, including satellite, wireless local-area networks, and ultralow power radios. He is currently a wireless specialist for low-power body area communication at the Cochlear Technology Center in Belgium.

Farshad Keshmiri (S'08) was born in Iran in 1982. He received the B.S. degree in electrical engineering and the M.S. degree in communication engineering from the Iran University of Science and Technology (IUST), Tehran, in 2004 and 2007, respectively. He is currently working toward the Ph.D. degree at the Ecole Polytechnique de Louvain, Université Catholique de Louvain (UCL), Belgium.

While at IUST, he concentrated on miniaturization of microwave antennas using electromagnetic bandgap (EBG) structures and implementation of some high gain EBG antennas. Since October 2007, he has been with the Laboratory of the Ecole Polytechnique de Louvain, UCL, where he has been working on the design of antennas devoting to the body area networks. His research interests include computational electromagnetics, body area networks, metamaterials and electromagnetic band gap antennas.

Gemma Roqueta Crusats was born in Girona, Spain, in 1983. She received the Telecommunication Engineer degree from Universitat Politècnica de Catalunya, Spain, in 2007, where she is working toward the Ph.D. degree.

In 2006, she was involved in body area networks research as a Visiting Student at the Université Catholique de Louvain, Belgium. Since September 2007, she is involved in developing microwave based non-destructive testing methods for monitoring and predicting civil infrastructure condition. Her research interest include indoor and outdoor propagation, wideband microwave imaging with spiralometric discrimination and ultrawideband antennas.

Christophe Craeye (M'08) was born in Belgium in 1971. He received the Electrical Engineer and Bachelor in Philosophy degrees in 1994 and the Ph.D. degree in applied sciences in 1998 from the Université Catholique de Louvain (UCL), Belgium.

From 1994 to 1999, he was a Teaching Assistant at UCL and carried out research on the radar signature of the sea surface perturbed by rain, in collaboration with the rain-sea interaction facility of NASA, Wallops Island, VA, and with the European Space Agency. From 1999 to 2001, was Postdoctoral Researcher at the Eindhoven University of Technology, The Netherlands. His research there has been carried out in the framework of the square kilometer array (SKA) radio telescope project, and consisted of studying a technology based on

phased-arrays traditionally used for broadband radar applications. In this framework, he was a Visiting Researcher at the University of Massachusetts in Fall 1999, and worked with the Netherlands Institute for Research in Astronomy (ASTRON) in 2001. Since 2002, he is an Associate Professor (Chargé de Cours) at UCL. His research interests are finite antenna arrays, multiple antenna systems and numerical methods for fields in periodic media, including metamaterials.

Proc. Craeye participates in the COST IC0603 Action on Antennas for Sensor applications funded by the European Commission. He is currently an Associate Editor of the IEEE TRANSACTIONS ON ANTENNAS AND PROPAGATION.

Claude Oestges received the M.Sc. degree and the Ph.D. degree in applied science from the Université Catholique de Louvain (UCL), Louvain-la-Neuve, Belgium, in 1996 and 2000, respectively.

From 1996 to 2000, he was an Assistant Lecturer in the Microwave Laboratory, UCL. From January to December 2001, he was a Postdoctoral Scholar in the Smart Antennas Research Group (Information Systems Laboratory) of Stanford University, CA. From October 2001 to September 2005, he was a Postdoctoral Fellow at the Belgian National Science Foundation FNRS (FRS-FNRS—Fonds de la Recherche Scientifique—FNRS), associated with the Microwave Laboratory UCL. He is presently a FRS-FNRS Research Associate and Assistant Professor at UCL. His research interests cover wireless and satellite communications, with a specific focus on the propagation channel and its impact on system performance. He is leading sub-working groups in COST 2100 "Pervasive mobile and ambient wireless communications" as well as in the Network of Excellence NEWCOM++. He is the author or coauthor of one book and more than 100 papers in international journals and conference proceedings.

Prof. Oestges was the recipient of the IEE Marconi Premium Award in 2001 and the IEEE Vehicular Technology Society Neal Shepherd Award in 2004. He currently serves as Associate Editor for the IEEE TRANSACTIONS ON VEHICULAR TECHNOLOGY and the *EURASIP Journal on Wireless Communications and Networking*.